

Photoreduction

Efficient and Selective Interplay Revealed: CO₂ Reduction to CO over ZrO₂ by Light with Further Reduction to Methane over Ni⁰ by Heat Converted from Light

Hongwei Zhang, Takaomi Itoi, Takehisa Konishi, and Yasuo Izumi*

Abstract: The reaction mechanism of CO₂ photoreduction into methane was elucidated by time-course monitoring of the mass chromatogram, in situ FTIR spectroscopy, and in situ extended X-ray absorption fine structure (EXAFS). Under ¹³CO₂, H₂, and UV/Vis light, ¹³CH₄ was formed at a rate of 0.98 mmol h⁻¹ g_{cat}⁻¹ using Ni (10 wt %)-ZrO₂ that was effective at 96 kPa. Under UV/Vis light irradiation, the ¹³CO₂ exchange reaction and FTIR identified physisorbed/chemisorbed bicarbonate and the reduction because of charge separation in/on ZrO₂, followed by the transfer of formate and CO onto the Ni surface. EXAFS confirmed exclusive presence of Ni⁰ sites. Then, FTIR spectroscopy detected methyl species on Ni⁰, which was reversibly heated to 394 K owing to the heat converted from light. With D₂O and H₂, the H/D ratio in the formed methane agreed with reactant H/D ratio. This study paves the way for using first row transition metals for solar fuel generation using only UV/Vis light.

Introduction

Photocatalytic CO₂ fuel conversion has been extensively examined to initiate a carbon neutral cycle using homogeneous or heterogeneous catalysts, which includes the use of solar fuel unlike the irreversible fossil fuel consumption^[1,2] and on-site fuel supply on planets.^[3] The conversion of CO₂ into methane, methanol, or formate can be achieved using metal complex-based photocatalysts; however, they require a sacrificial reductant^[4,5] and in most cases deactivate in a few hours.^[6] However, the CO₂ conversion performed using heterogeneous photocatalysts is often stable and does not require a sacrificial reductant. Nevertheless, the product obtained is CO, which is an essential raw chemical but not a fuel,^[1,2,7-9] unlike the ethene or ethanol produced if electricity is applied.^[10-12]

Previously, studies rarely clarified a steady-state reaction mechanism for converting CO₂ to solar fuel especially using

How to cite: *Angew. Chem. Int. Ed.* **2021**, *60*, 9045–9054

International Edition: doi.org/10.1002/anie.202016346

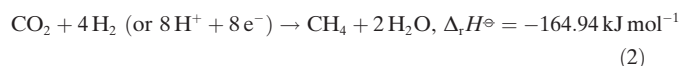
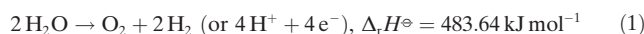
German Edition: doi.org/10.1002/ange.202016346

¹³C-labelled reactant, which led to a misunderstanding of nonsteady-state reactions.^[1,13,14] Although the mass spectrometry (Supporting Information, Figure S1A) of the photocatalytic product or both mass spectrometry and mass chromatography (Figure S1B) using ¹³CO₂ have been extensively reported,^[15-17] these data are available at one timepoint in a kinetic study and the steady-state information has rarely been reported.^[18]

The operating mechanism of reaction steps comprising photocatalysis is often uncertain. This study demonstrates a steady-state photoconversion of CO₂ into methane using a composite of ZrO₂ and Ni⁰ nanocrystals through the time-course monitoring of online mass chromatogram (time course of Figure S1B) of an isotope-labeled solar fuel (¹³CH₄) produced from ¹³CO₂ using only UV/Vis light. We reported CO₂ photoreduction to CO over ZrO₂ surface assisted by H₂ activation and spillover from Ag^[19] or Au nanoparticles.^[20] Moreover, photocatalytic CO formation from CO₂ was reported using ZrO₂^[21-23] and Cu-ZrO₂.^[24]

However, a Ni-ZrO₂ photocatalyst converts CO₂ to CO over a ZrO₂ surface owing to a charge separation by UV/Vis light followed by hydrogenation of CO into methane over a Ni nanoparticle surface using heat (394 K) converted from light energy. Such an interplay in photocatalyst composites has been speculated for various photocatalytic reactions but has been revealed for the first time through the in situ temperature monitoring of Ni sites under UV/Vis light by extended X-ray absorption fine structure (EXAFS). The concerted mechanism does not proceed by heat only, i.e., in the absence of the first photoreduction step from CO₂ into CO over ZrO₂.

Among reaction steps from CO₂ to methane [Eqs. (1)–(3)], we first evaluate the reaction rate of the exothermic Step 2 [Eq. (2)], which follows the photo-oxidation of water in Step 1 (eq. 1). Finally, we attempt the photoconversion of ¹³CO₂ into methane using moisture (Step 3).



Results and Discussion

We examined the samples for ¹³CO₂ photoreduction (Table 1a–e). ZrO₂ previously reduced in H₂ at 723 K

[*] Dr. H. Zhang, Prof. Dr. T. Konishi, Prof. Dr. Y. Izumi
Department of Chemistry
Graduate School of Science, Chiba University
Yayoi 1–33, Inage-ku, Chiba 263-8522 (Japan)
E-mail: yizumi@faculty.chiba-u.jp

Prof. Dr. T. Itoi
Department of Mechanical Engineering
Graduate School of Engineering, Chiba University
Yayoi 1–33, Inage-ku, Chiba 263-8522 (Japan)

Supporting information and the ORCID identification number(s) for the author(s) of this article can be found under:
https://doi.org/10.1002/anie.202016346.

Table 1: Kinetic data on photoconversion of $^{13}\text{CO}_2$ using H_2 and the H_2 -pretreated ZrO_2 - and SiO_2 -based photocatalysts (0.020 g).^[a]

Entry	Catalyst	$^{13}\text{CO}_2$ [kPa]	H_2 [kPa]	Light irradiated	Formation rate of C-containing products [$\mu\text{mol h}^{-1} \text{g}_{\text{cat}}^{-1}$]					^{12}C product ratio [mol%]
					^{13}CO	^{12}CO	$^{13}\text{CH}_4$	$^{12}\text{CH}_4$	Σ C-containing products	
a	ZrO_2 -Reduced				1.9	0.086	<0.002	<0.002	2.0	4.3
b	Ni (5.0 wt %)- ZrO_2 -Reduced	2.3	21.7		0.027	<0.002	21	0.44	22	2.0
c				Full light	0.15	<0.002	320	14	340	4.3
c'					0.54	<0.002	980	79	1060	7.5
c''		4.6	43.4		0.38	<0.002	740	47	780	6.0
c'''		9.2	86.8		0.37	<0.002	700	30	730	4.1
c''''	Ni (10 wt %)- ZrO_2 -Reduced			$\lambda > 320$ nm	0.049	<0.002	69	1.5	71	2.1
c'''''				$\lambda > 520$ nm	0.007	<0.002	18	1.1	19	5.7
c''''''				$\lambda > 715$ nm	<0.002	<0.002	0.24	0.049	0.29	29
c'''''''				No light	<0.002	<0.002	0.053	0.027	0.080	34
c''''''''				Full light, 295 K bath	<0.002	<0.002	0.15	0.014	0.16	8.5
d	Ni (15 wt %)- ZrO_2 -Reduced	2.3	21.7		0.084	<0.002	130	4.8	140	3.5
e	Ni (30 wt %)- ZrO_2 -Reduced			Full light	0.023	<0.002	1.3	0.054	1.3	4.0
f	Ni (10 wt %)- SiO_2 -Reduced				0.27	<0.002	0.26	0.035	0.57	6.2

[a] Irradiated under UV/Visible light @142 mWcm^{-2} except for c', c'', c''', and c'''''' (186 mWcm^{-2}).

(ZrO_2 -Reduced) exclusively formed CO (Figure 1A). The CO formation remained steady for ca. 18 h and the rate decreased by 14% at 28 h (Figure 1A, right).

In clear contrast, Ni- ZrO_2 previously reduced in H_2 at 723 K (Ni- ZrO_2 -Reduced) samples mostly produced CH_4 with a molar ratio of >98% (Table 1b–e) and CO as the minor product. The switching of the photoproduct from CO to methane by typically doping noble metals on TiO_2 has been reported,^[1,2] where the valence state of metals under photocatalytic reaction conditions is the key factor rather than the work function of metals suggested in the literature.^[2,25]

By varying the Ni content between 5.0 and 30 wt% in Ni- ZrO_2 -Reduced, the formation rate of C-containing products reached a maximum with Ni 10 wt% ($340 \mu\text{mol h}^{-1} \text{g}_{\text{cat}}^{-1}$; Figures 1C and S3), which was higher than the rate obtained using ZrO_2 -Reduced by a factor of 170 times (Table 1a,c). The reason why the rate drew a maximum curve is discussed in the Supporting Information, EXAFS section. Using Ni- ZrO_2 -Reduced photocatalysts, the methane formation rates remained constant until 27–48 h and decreased by 0–13% at 48–49 h of the reaction (Figure 1B–E). The equilibrium of the exothermic reaction [Eq. (2)] was preferably balanced to the products thermodynamically, and the 33% decrease of rate after 48 h of reaction using Ni (10 wt %)- ZrO_2 -Reduced did not result from photocatalyst deactivation but from the almost total consumption of the reactant $^{13}\text{CO}_2$ (Figure 1C).

At 723 K, the pretreatment under H_2 was essential for CO_2 photoreduction using Ni- ZrO_2 -Reduced (Table 1b–e). The methane formation rate using Ni (10 wt %)- ZrO_2 ($3.2 \mu\text{mol h}^{-1} \text{g}_{\text{cat}}^{-1}$, Table S1b), i.e., not H_2 -treated, was only 0.94% of that using Ni (10 wt %)- ZrO_2 -Reduced (Figure 1C and Table 1c) owing to the difference in Ni^{II} versus Ni^0 states.

The ^{12}C ratio in C-containing compounds generated using ZrO_2 -Reduced and Ni (5.0–30 wt %)- ZrO_2 -Reduced was 2.0–4.3 mol% (Table 1a–e), which was greater than the ratio of ^{12}C contained in the $^{13}\text{CO}_2$ reaction gas (1.0%). To understand the inconsistency, $^{13}\text{CO}_2$ uptake/exchange tests were conducted under UV/Vis light irradiation. Using ZrO_2 -Reduced and $^{13}\text{CO}_2$ (56.7 μmol), 9.9 μmol of CO_2 gas very quickly adsorbed at a rate constant of 8.0 h^{-1} with the $^{13}\text{CO}_2$ / $^{12}\text{CO}_2$ molar ratio of 99:1 (Figure 2A). Then, a slower $^{13}\text{CO}_2$ / $^{12}\text{CO}_2$ exchange reaction proceeded at a rate constant of 0.07 h^{-1} , illustrated by the gradual increase in $^{12}\text{CO}_2$ for 24 h (Figure 2A).

Moreover, the $^{13}\text{CO}_2$ photo-uptake/exchange was tested using Ni (10 wt %)- ZrO_2 -Reduced (Figure 2B). The initial uptake amount of CO_2 reduced by 40% (5.9 μmol) compared to ZrO_2 -Reduced (Figure 2A). Furthermore, the rate constant was smaller (3.0 or 0.4 h^{-1}) than that of 8.0 h^{-1} obtained using ZrO_2 -Reduced, suggesting both a physical block and kinetic interference by Ni nanocrystals for CO_2 adsorption on ZrO_2 .

Based on the $^{12}\text{CO}_2$ ratio (2.4 and 2.1 mol%) in the equilibrated CO_2 gas (Figure 2), the $^{12}\text{CO}_2$ amounts existing prior to the photouptake/exchange test on ZrO_2 -Reduced and Ni (10 wt %)- ZrO_2 -Reduced were 0.79 and 0.64 μmol (Supporting Information). Therefore, the equilibrated $^{12}\text{CO}_2$ ratios during the photocatalytic reduction tests using 2.3 kPa of $^{13}\text{CO}_2$ (193 μmol), including an impurity of $^{12}\text{CO}_2$ (1.9 μmol), were 1.4 and 1.3 mol%, respectively (Supporting Information). However, the ^{12}C ratios in the CO produced using ZrO_2 -Reduced and CH_4 produced using Ni (10 wt %)- ZrO_2 -Reduced were both 4.3 mol% (Table 1a, c) and negligibly changed during the test (Figure 1A, C). Thus, a relatively stronger adsorption site for CO_2 over ZrO_2 was an active site

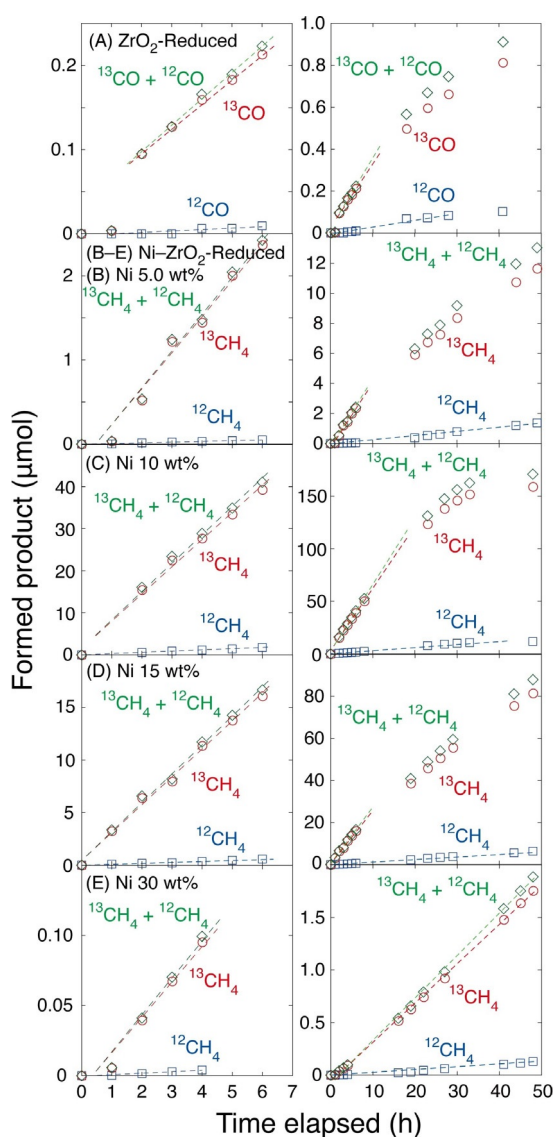


Figure 1. Time course of A) ^{13}CO and ^{12}CO and B–E) $^{13}\text{CH}_4$ and $^{12}\text{CH}_4$ formation during the photocatalytic test exposed to $^{13}\text{CO}_2$ (2.3 kPa) and H_2 (21.7 kPa) using A) ZrO_2 -Reduced, B) Ni (5.0 wt%)- ZrO_2 -Reduced, C) Ni (10 wt%)- ZrO_2 -Reduced, D) Ni (15 wt%)- ZrO_2 -Reduced, and E) Ni (30 wt%)- ZrO_2 -Reduced. The amount of catalyst was 0.020 g.

for the reduction to CO (Scheme 1A-c).^[19,20] Previously, O vacancy site (Zr^{3+}) was suggested for the reduction to CO based on electron paramagnetic resonance.^[22] The O vacancy sites increased by 1.46 times by the H_2 pretreatment of ZrO_2 at 723 K, accounting for the increase of CO formation rate by 1.16 times (Tables 1a and S1a; Supporting Information).

Pressure dependence was evaluated by increasing the light intensity (142 mW cm^{-2}) applied in all the experiments to 186 mW cm^{-2} (Table 1c', c'', c'''). By increasing the pressure of $^{13}\text{CO}_2$ and H_2 by two and four times, methane formation rates decreased by 26% and 31%, respectively, but the formation was always steady until the $^{13}\text{CO}_2$ was consumed. Thus, the effect of adsorption inhibition by CO_2 for the transfer of formate/CO to Ni^0 was moderate, and Ni- ZrO_2 -Reduced was applicable near the atmospheric pressure.

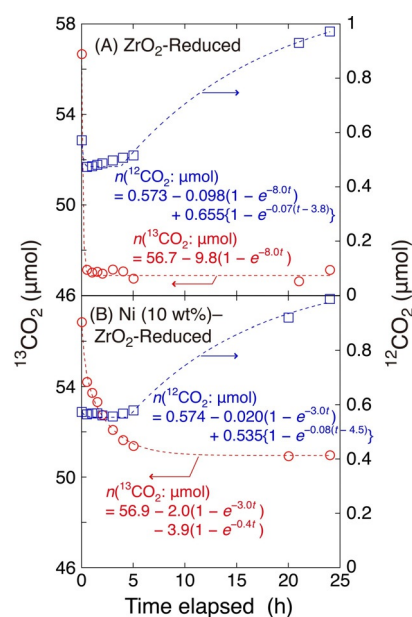
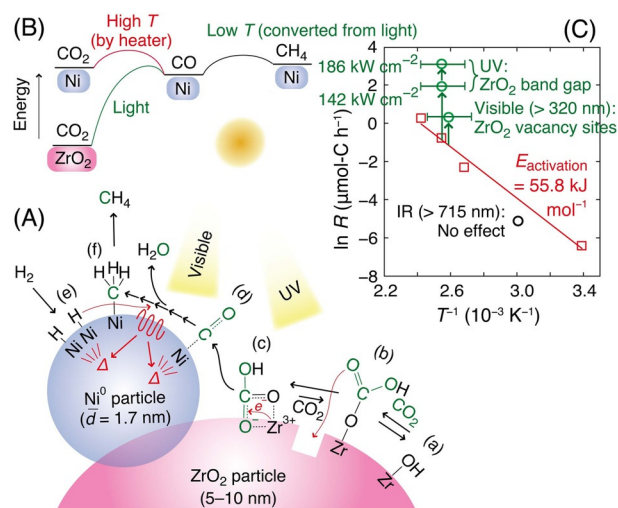


Figure 2. Time-course uptake and exchange reaction of $^{13}\text{CO}_2$ (0.67 kPa) irradiated by UV/Vis light using A) ZrO_2 -Reduced and B) Ni (10 wt%)- ZrO_2 -Reduced. The amount of catalyst was 0.020 g.



Scheme 1. A) Proposed intermediate species during CO_2 exchange and photocatalytic CO_2 reduction, B) the energetics, and C) the rate comparison to heat reactions.

Approximately zero order kinetics were reported for Ag- ZrO_2 under similar pressure range.^[19]

Next, the effects of the excitation light wavelength were investigated using the most active Ni (10 wt%)- ZrO_2 -Reduced photocatalyst (Figure S4A-C and Table 1c''', c''', c'''). The formation rates of C-containing products irradiated by light at wavelengths $\lambda > 320 \text{ nm}$, $\lambda > 520 \text{ nm}$, and $\lambda > 715 \text{ nm}$ (Figure S6) were 21%, 5.6%, and 0.086% of that irradiated by full light, respectively (Figure 1C and Table 1c). Furthermore, the methane formation rate in the kinetic test under dark conditions at 298 K was even smaller: 0.024% (Table 1c''''') of that irradiated by full light. The dark

reaction was not effectively catalytic because the CH₄ formation slowed down after 10 h of the reaction to deactivate (Figure S4D, right) owing to the oxidation of the Ni surface by CO₂. Thus, the contribution of light for CO₂ conversion was 79% ($\lambda < 320$ nm), 15% ($320 < \lambda < 520$ nm), 5.5% ($520 < \lambda < 715$ nm), 0.06% ($\lambda > 715$ nm), and 0.02% (heat reaction).

The gradual increase of ¹²C-product ratio from 4.3 to 34 mol% as the minimum wavelength of irradiated light increases (Table 1c, c''', c''''', c''''''', c''''''''') indicates that the light of shorter wavelength mostly activates CO₂ strongly adsorbed on ZrO₂ (¹²CO₂ in early stage of reaction; Scheme 1A-c) via major band-gap and minor mid-band excitations (Figure 5; Supporting Information).

For comparison, the Ni (10 wt%)-SiO₂ catalyst previously reduced in H₂ at 723 K [Ni (10 wt%)-SiO₂-Reduced] was tested for CO₂ photoconversion under ¹³CO₂, H₂, and full UV/Vis light (Figure S5A). CO and methane were formed at 0.27 and 0.30 μmol h⁻¹ g_{cat}⁻¹, respectively; however, the total rate was 0.17% of that obtained using Ni (10 wt%)-ZrO₂-Reduced (Table 1c, f). Other control kinetic tests were performed using Ni (10 wt%)-ZrO₂-Reduced in dark conditions at 373–413 K. The obtained Arrhenius plot is shown in Scheme 1C. The formation rates of the C-containing products, which were mostly methane at 373, 393, and 413 K were 1.4%, 6.6%, and 18%, respectively, as a percentage of that obtained on irradiation by full light at 142 kW cm⁻².

The photocatalytic methane formation was reported from CO₂ and H₂ using Ni-SiO₂-Al₂O₃ with no heat supply from surroundings.^[26] The transformation of light energy into heat on Ni appeared to be similar; however, the contribution of charge separation in ZrO₂ is in contrast to that in SiO₂-Al₂O₃.

To obtain further insight into the mechanism of CO₂ photoreduction to methane, Fourier transform infrared (FTIR) spectra were measured for Ni (10 wt%)-ZrO₂-Reduced. ¹³CO₂ was used to distinguish the species formed from atmospheric ¹²CO₂.^[19,20] The isotopic shift was calculated using harmonic oscillation from Equations (4)–(6):

$$\tilde{\nu} = \frac{1}{2\pi c} \sqrt{\frac{k}{\mu}} \quad (4)$$

$$\frac{\tilde{\nu}_{13\text{CH}}}{\tilde{\nu}_{12\text{CH}}} = \frac{\sqrt{\frac{1}{13} + \frac{1}{1}}}{\sqrt{\frac{1}{12} + \frac{1}{1}}} = 0.99704 \quad (5)$$

$$\frac{\tilde{\nu}_{13\text{CO}}}{\tilde{\nu}_{12\text{CO}}} = \frac{\sqrt{\frac{1}{13} + \frac{1}{16}}}{\sqrt{\frac{1}{12} + \frac{1}{16}}} = 0.97778 \quad (6)$$

where $\tilde{\nu}$ is the wave number, c is the speed of light, k is the force constant, and μ is the reduced mass.

With the adsorption of ¹³CO₂ (2.3 kPa) and H₂ (21.7 kPa) at 295 K for 1 h, peaks appeared at 1588, 1389, and 1220 cm⁻¹ and were assigned to the frequency modes of antisymmetric stretching vibration $\nu_{\text{CO}_2(\text{as})}$, symmetric stretching vibration $\nu_{\text{CO}_2(\text{s})}$, and bending vibration δ_{OH} of bicarbonate species, respectively (monodentate or bridging; Figure S7A). The peaks at 1624, 1421, and 1220 cm⁻¹ correspond to ¹²C-

bicarbonate species according to eq. 6, and agree with the results available in literature.^[19,20,27,28] Simultaneously, the ν_{OH} peak intensity at 3700 cm⁻¹ of ZrO₂ decreased owing to the reaction with CO₂ (Scheme 1A-a, b), whereas the ν_{OH} peak intensity of the frequency mode of bicarbonate increased at 3615 cm⁻¹ (Figure S7A).

Weaker shoulder peaks, owing to the frequency modes of $\nu_{\text{CO}_2(\text{as})}$ and $\nu_{\text{CO}_2(\text{s})}$ of the carbonate species, appeared at 1509 and 1304 cm⁻¹, respectively (Figure S7A). These positions were in agreement with the ¹²CO₃ species based on eq. 6 (1543 and 1334 cm⁻¹), as well as with literature.^[19,20,28,29] However, no distinguishable peaks were observed in the ν_{CO} or ν_{CH} region (Figure 3A).

We then monitored the FTIR spectroscopy changes associated with UV/Vis light irradiation (Figures 3B and S7B). Two intense peaks (2940 and 2857 cm⁻¹) and a weak peak (2750 cm⁻¹) gradually grew in the ν_{CH} region (Figure 3B). The values corresponded to 2949, 2865, and 2758 cm⁻¹ for ¹²CH stretching vibration, calculated using Equation (5), and could be assigned to $\nu_{\text{CH}(\text{as})}$ and $\nu_{\text{CH}(\text{s})}$ of ¹³CH₃ on Ni⁰ (Scheme 1A-f) and ν_{CH} of ¹³C-formate.^[28,30] Because formed ¹³CH₄ diffuses both in IR cell and Pyrex glass circulation system (Supporting Information), the IR active ν_{CH} (3010 cm⁻¹) and δ_{CH} (1302 cm⁻¹) peaks^[31] for ¹³CH₄ were not clearly detected. Instead, CH₄ was quantified by gas chromatography-mass spectrometry (GC-MS, see below).

In the ν_{CO} region, a peak gradually appeared at 2017 cm⁻¹ (Figure 3B, right) and was assigned to CO on Ni⁰ (Scheme 1A-d).^[32] Any peaks in ν_{CH} and ν_{CO} regions (Figure 3B) did not appear in the FTIR spectra for ZrO₂ (Figure S8), demonstrating that the methyl and CO species were over Ni⁰. Formate was formed at the interface between the ZrO₂ and Ni⁰ surfaces by a two-electron reduction of bicarbonate (Scheme 1A-b, c), followed by transformation to CO on the Ni⁰ surface and the hydroxy group of ZrO₂. Based on the ¹²CH₄ ratio (2.0–4.3 mol%) using Ni-ZrO₂-Reduced irradiated under full light significantly increased from the ¹²C ratio in the reactant (1.0 mol%), methane formation starting from CO₂ exclusively over Ni⁰ surface is not plausible because ¹²C in ¹²CH₄ was derived from ZrO₂ surface, not from clean Ni⁰ surface. Furthermore, heat reaction at 393 K under dark conditions mostly over Ni⁰ surface was very slow compared to light reaction (see the final part and Scheme 1), demonstrating that CO₂ reduction to CO mostly occurred over ZrO₂ surface.

In the ν_{CO_2} region under UV/Vis light, new peaks at 1530 and 1340 cm⁻¹ gradually increased (Figure S7B, right) in compensation of the bicarbonate peaks at 1588, 1389, and 1220 cm⁻¹ (Figure S7A, right) decreased. The new peaks could be assigned to $\nu_{\text{CO}_2(\text{as})}$ and $\nu_{\text{CO}_2(\text{s})}$ of a bidentate formate. The calculated values (1565 and 1370 cm⁻¹, respectively) for ¹²C-formate based on eq. 6 were in agreement with the literature.^[27] Then, with the light turned off and under vacuum, the peaks ascribed to formate became dominant and that at 1382 cm⁻¹ was resolved owing to the δ_{CH} of formate, which corresponded to 1386 cm⁻¹ for the ¹²C-formate species based on Equation (5).^[28]

The gradual increase in intensity for the $\nu_{\text{CH}(\text{s})}$ peak of ¹³CH₃ on Ni⁰ under light (Figure 3B) corresponded to the

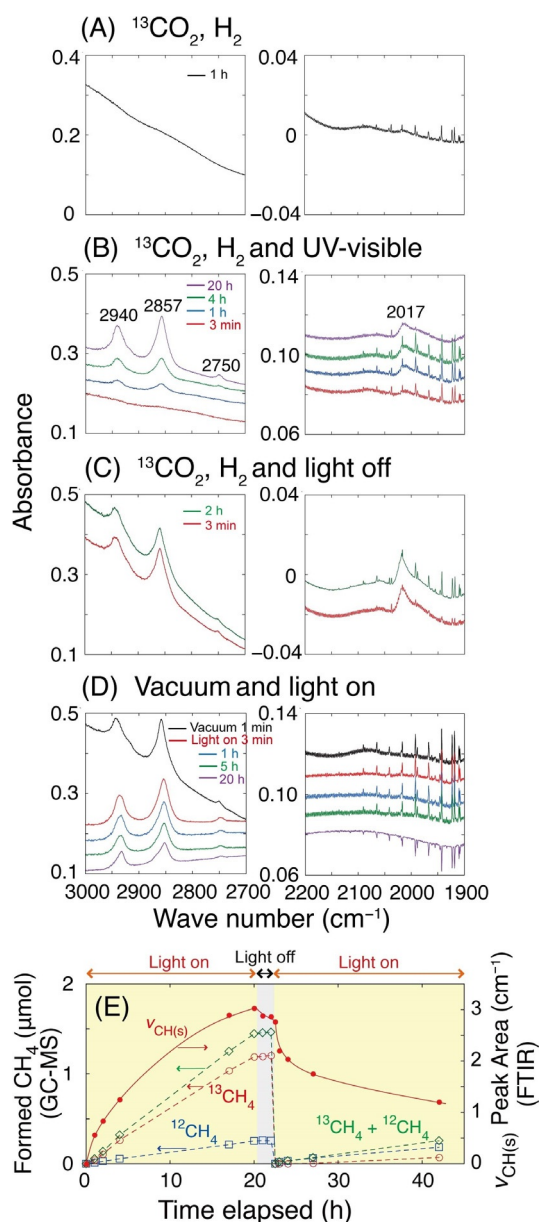


Figure 3. A)–D) FTIR spectra of Ni (10 wt%)-ZrO₂-Reduced (10 mg) for 3000–2700 cm⁻¹ (left) and 2200–1900 cm⁻¹ (right). The spectrum for Ni (10 wt%)-ZrO₂ just reduced in H₂ at 723 K was subtracted from each data. A) Under ¹³CO₂ (2.3 kPa) and H₂ (21.7 kPa) for 1 h. B) Under ¹³CO₂, H₂, and UV/Vis light for 20 h. C) Under ¹³CO₂, H₂, and darkness for 2 h. D) Under vacuum for 1 min, and then UV/Vis light for 20 h. E) Correlation between methane formed by GC-MS and ν_{CH(s)} peak area owing to CH₃ species by FTIR.

amount of formed methane simultaneously monitored by GC-MS (Figure 3E). This fact suggests that the hydrogenation of the methyl species on the Ni⁰ surface (Scheme 1A-f) was a relatively slow step. The methyl species slowly decreased when the light was turned off (Figure 3C,E). Under irradiation by UV/Vis light in vacuum for 1 min, a significant portion of the methyl, CO, formate, and bicarbonate species decomposed (Figures 3C,D and S7C,D) and a slower methane formation from methyl species

combined with H occurred on the Ni⁰ surface (Figure 3E and Scheme 1A-e, f).

In the transmission electron microscopy (TEM) image of Ni (10 wt%)-ZrO₂, ca. 10 nm of crystal was observed (Figure 4A). On further inspection, a 5–10 nm crystal showing a lattice fringe with an interval of 0.194 nm, assignable to monoclinic ZrO₂ (202) plane, was connected to ca. 20 nm of crystal, showing a lattice fringe with an interval of 0.299 nm, assignable to the monoclinic ZrO₂ (111) plane (theoretical 0.285 nm, Figure 4B). The other crystal showing a lattice fringe with an interval of 0.314 nm, assignable to the monoclinic ZrO₂ (111) plane (theoretical 0.318 nm), was further connected. Similarly, crystals showing lattice fringes with intervals of 0.275–0.280, 0.314, and 0.258 nm were observed (Figure 4C), assignable to monoclinic ZrO₂ (111), (111), and (200) planes [theoretical 0.255 nm for (200)], respectively.^[33,34]

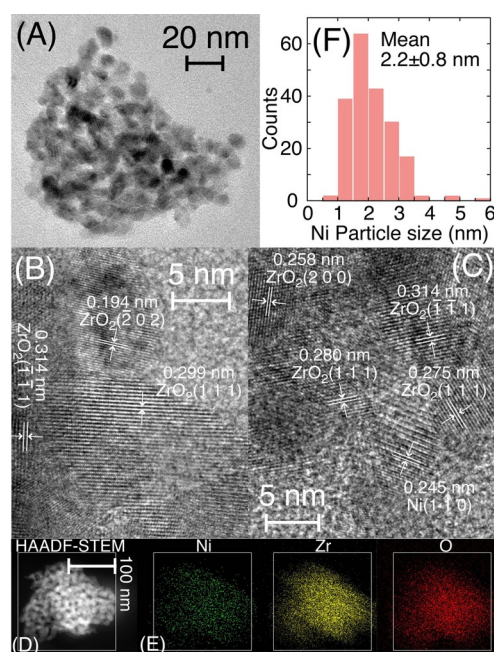


Figure 4. A) TEM, B),C) HR-TEM, and D) HAADF-STEM images observed for Ni (10 wt%)-ZrO₂-Reduced sample. E) Associated energy-dispersive spectrum mapping for X-ray fluorescence of Ni Lα, Zr Lα, and O Kα. F) Histogram of Ni nanoparticle size based on TEM and HAADF-STEM. The crystal face indexes for ZrO₂ are of monoclinic phase.

Furthermore, smaller spheres/spheroids were found attached on ZrO₂ crystals as darker and brighter images in TEM and higher-angle annular dark-field (HAADF)-scanning TEM (STEM), respectively (the arrows in Figure S9A, B). Then, a spherical crystal with a lattice fringe interval of 0.245 nm, assignable to the Ni (110) plane (theoretical 0.249 nm)^[35] connected to the monoclinic ZrO₂ (111) crystals, was visible (Figure 4C). It was relatively difficult to identify Ni crystals despite the high content (10 wt%), indicating that most Ni crystals were smaller than the ZrO₂ crystals, which corresponds to a weak X-ray diffraction (XRD) peak assigned to Ni (111) (Figure S10). Moreover, this corresponds

to the distribution of Ni, Zr, and O in the X-ray fluorescence mapping (Figure 4E) compared to the spatial distribution of crystals in HAADF-STEM (Figure 4D). Based on high-resolution (HR)-TEM and HAADF-STEM images, the Ni particle size distribution was obtained with a mean of 2.2 ± 0.8 nm (Figure 4F).

The fluorescence spectra were measured for Ni-ZrO₂-Reduced samples at an excitation wavelength of 200 nm, which is below the band gap wavelength (248 nm) of ZrO₂ (Figure S6).^[19,20] The broad fluorescence band centered at 370 nm with a half width of 120 nm agreed with the data previously reported for ZrO₂ nanocrystals (mean 2.9 nm).^[36] Moreover, a sharp peak at 396 nm appeared in the ZrO₂ spectrum (Figure 5A). The emission in this range is attributed to the short-wavelength excitation on the near band-edge transitions, whereas the peaks at 530 and 625 nm are attributed to the excitation to the mid-gap trap states, e.g., surface O vacancy.^[37]

As the Ni content gradually increased, the progressive decrease in fluorescence intensity was much quicker for Ni (0–30 wt %)-ZrO₂-Reduced samples (Figure 5A) than that for the non-H₂-pretreated samples (Figure S11A). A part of the reasons of the fluorescence peak decrease was the charge transfer from conduction band of ZrO₂ (-1.0 V)^[19] to Ni (Fermi level 0.60–0.91 V).^[35] The accelerated hydrogenation steps over Ni⁰ can be expected owing to the transferred electrons from ZrO₂ (Scheme 1 A-d-f).

Figure 5B shows the excitation spectra for ZrO₂ and Ni (10 wt %)-ZrO₂-Reduced, where the dependence is essentially equivalent for the fluorescence peaks at 370 (red line) and 396 nm (blue line). The emission below 248 nm was attributed to the relaxation of the band gap excitation;

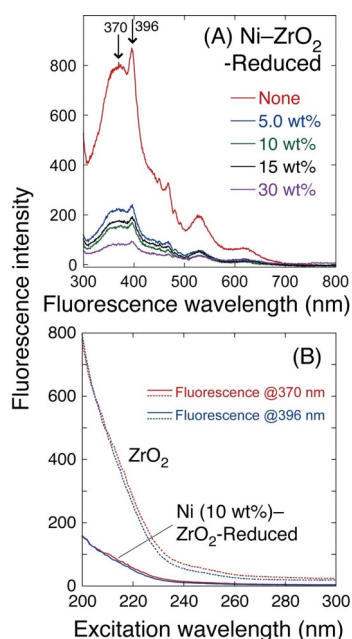


Figure 5. Fluorescence spectra for Ni (0–30 wt %)-ZrO₂-Reduced with the excitation at 200 nm (A) and excitation spectra for ZrO₂ and Ni (10 wt %)-ZrO₂-Reduced (B); 2 mg of the sample powder was suspended in 3 mL of water.

however, the weaker fluorescence above 248 nm was caused by the low concentration of O vacancy level between the ZrO₂ band gaps. As already shown for the excitation at 200 nm (Figure 5A), the fluorescence was extensively suppressed by 10 wt % Ni and became negligible in the excitation wavelength range of > 248 nm.

Xe arc lamps and quartz sample cells enabled UV light below 248 nm in ¹³CO₂ kinetic tests and fluorescence spectroscopy (Figures 1, 5, S2, and S11; Experimental section, Supporting Information), leading to the highest ¹³CH₄ formation rate based on ZrO₂ band gap (Table 1c). In contrast, the light absorption above 248 nm due to interband states, e.g., surface O vacancy of ZrO₂^[37] and subsequent electron transfer to Ni were indirectly confirmed based on the excitation spectra (Figure 5B), leading to the ¹³CH₄ formation rate under light of > 320 nm, 22 % of the rate under full light.

The importance of this study is steady CO₂ conversion into methane using Ni-ZrO₂-Reduced and UV/Vis light, no heat applied from surroundings (see below). However, the rate is suppressed to 20–30 % (see below for the reaction using water) using sunlight reached on the earth surface, filtered by O₂ and ozone layer.^[38,39] To fully utilize the performance of Ni (10 wt %)-ZrO₂-Reduced (Table 1c, c'), the applications in the area affected by O₃ layer depletion that allows UV light below 248 nm,^[39–41] at 25–50 km high in the O₃ layer (CO₂ < 1 Pa,^[42] H₂O < 0.03 Pa^[43]) to increase O₂ via Equation (1) to mitigate O₃ depletion by the O₂ photodissociation, and as on-site fuel supply on Mars (43 % of sunlight flux compared to the earth^[38,44]) where UV light below $\lambda < 300$ nm is negligibly filtered due to the composition of atmosphere (95 % CO₂, 3 % N₂, and a few water).^[45]

Next, the variation in the Ni K-edge EXAFS for Ni (10 wt %)-ZrO₂-Reduced photocatalyst, irradiated by UV/Vis light, was monitored. The Fourier transform showed a typical pattern for metallic Ni sites before light irradiation (Figure 6A). However, the major peak intensity at 0.21 nm (phase shift uncorrected) quickly decreased to 78 % within 20 min of irradiation and essentially remained the same for 130 min. The peak intensity ratio did not change throughout the monitoring and no new peaks appeared (Figure 6A, B), demonstrating the Ni⁰ state unchanged (Scheme 1 A). Then, the reason for the decrease in peak intensity was investigated. The time course changes of the major fit parameters, coordination number *N* and Debye-Waller factor σ , for the Ni-Ni interatomic pair are illustrated in Figures 6C and D, respectively.

The σ value was calculated as 0.00492 nm for Ni metal at 295 K based on the correlated Debye model^[46,47] using ab-initio multiple-scattering calculation code FEFF8.4^[48] and the Debye temperature of Ni [$\theta_{\text{Debye(bulk)}}$ 450 K].^[49] The XDAP code^[50] provided the experimental difference for the σ^2 value of the Ni metal (model) based on Equation (7).

$$A_j(k) = \frac{N_j}{kR_j^2} |f_j(k)| \exp \left[-2 \left(\sigma_j^2 k^2 + \frac{R_j}{\lambda} \right) \right], j = \text{Nickel} \quad (7)$$

in which $A_j(k)$, f_j , and R_j are amplitude, backscattering amplitude, and interatomic distance, respectively, for shell *j*, *k*

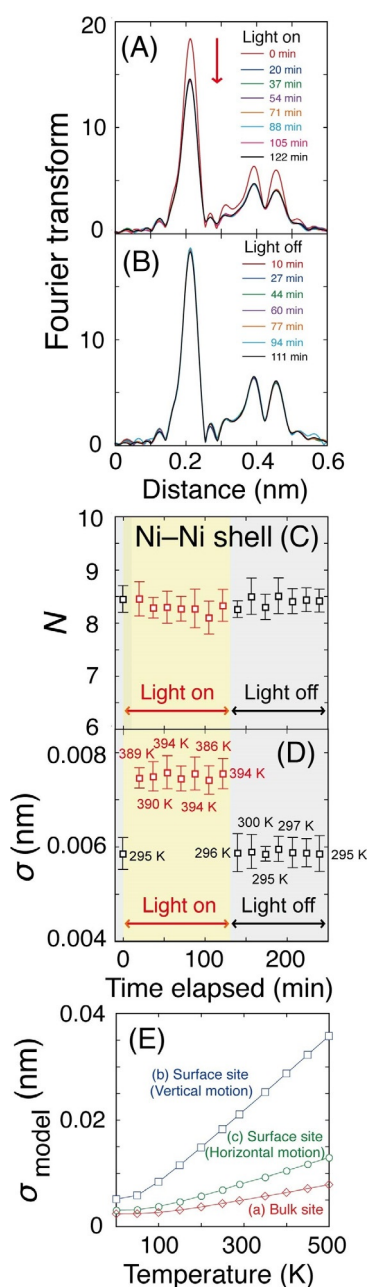


Figure 6. Ni K-edge EXAFS for Ni (10 wt%)-ZrO₂-Reduced (0.12 g) under CO₂ (2.3 kPa) and H₂ (21.7 kPa). A), B) Time-course change in Fourier transform of $k^3\chi$ irradiated by light from Xe arc lamp (A) and under dark (B). C), D) N (C) and σ values (D) obtained by curve-fit analyses of the Ni-Ni shell at 0.21 nm in (A) and (B). E) Temperature dependence of σ of the bulk site (a) and surface site for vertical and horizontal motions to the surface (b, c) calculated using the FEFF8.4 code.^[48]

is the angular photoelectron wavenumber, and λ is the mean free photoelectron path.

Furthermore, we consider that the contribution of structural disorder for the σ value^[51] is the difference of the σ^2 value from the Ni metal.

$$\sigma^2 = \sigma_{\text{correlated_Debye}}^2 + \Delta(\sigma_{\text{disorder}}^2) + \Delta(\sigma_{\text{XDAP}}^2) \quad (8)$$

To adjust the theoretical temperature estimated for the Ni (10 wt %)-ZrO₂ sample measured at 295 K, the σ_{disorder} value was evaluated as 0.00313 nm.

Apparently, the $N(\text{Ni-Ni})$ value negligibly changed within 8.3 ± 0.2 (Figure 6C) during light irradiation, whereas the $\sigma(\text{Ni-Ni})$ value quickly increased from 0.00585 nm before irradiation to 0.00745 nm within 20 min of irradiation, and remained at 0.00751 ± 0.00008 nm (Figure 6D).

Then, the UV/Vis light was turned off. Although the Fourier transform and the $N(\text{Ni-Ni})$ value remained approximately the same, at 8.4 ± 0.2 for 111 min (Figure 6B, C), the $\sigma(\text{Ni-Ni})$ value quickly decreased to 0.00587 nm within 10 min and remained within 0.00589 ± 0.00004 nm for 111 min (Figure 6D). Separately, the $N(\text{Ni-Ni})$ value was 8.4 ± 0.2 based on the analysis of the Ni (10 wt %)-ZrO₂-Reduced sample after 48 h of reaction under ¹³CO₂, H₂, and UV/Vis light, which suggests that the Ni particle size only changes negligibly after a two-day reaction.

We evaluated the temperature at Ni sites based on σ values. The σ value temperature dependence was derived from FEFF8.4,^[48] combined with the correlated Debye model,^[46,47] for Ni sites using the values of $\theta_{\text{Debye}}(\text{bulk})$ 450 K,^[49] $\theta_{\text{Debye}}(\text{Surf.,}\perp)$ 208 K, and $\theta_{\text{Debye}}(\text{Surf.,}\parallel)$ 348 K^[52] for bulk sites and the motion of vertical and horizontal freedom of translation, respectively, assuming face-centered cubic (fcc) Ni (111) surface sites (Figure 6E).

Based on the mean $N(\text{Ni-Ni})$ value (8.3) for Ni (10 wt %)-ZrO₂ (Figure 6C) and assuming a fcc nanocluster model exposing the preferred (111) face,^[53,54] a mean particle size of 1.7 nm and a dispersion (D) of 0.64 were evaluated. Moreover, we approximated the mean Ni nanoparticle temperature as the arithmetic mean value based on $\theta_{\text{Debye}}(\text{Surf.,}\perp)$ weighted by $1/2 \cdot 1/3D$ and $\theta_{\text{Debye}}(\text{Surf.,}\parallel)$ weighted by $1/2 \cdot 2/3D$ for vertical and horizontal translational motions at a free hemisphere surface and $\theta_{\text{Debye}}(\text{bulk})$ weighted by $1 - 1/2D$ (bulk site and non-free hemisphere in contact with ZrO₂).

Thus-evaluated temperature of Ni is indicated in the time course of Figure 6D. The initial temperature of Ni sites (295 K) quickly increased to 389 K within 20 min after the UV/Vis light irradiation began and remained essentially constant (389–394 K) during light irradiation for 130 min. When the UV/Vis light was turned off, the temperature suddenly decreased to 296 K within 10 min.

The methane formed during the initial 20 min of full light irradiation over the Ni (10 wt %)-ZrO₂ photocatalyst (Table 1c and Figure 6D) was 3.4 μmol , corresponding to the heat of reaction of 0.56 J (Eq. (2)). Based on the molar heat capacity of Ni and ZrO₂ ($C_{\text{p,m}}^\ominus = 26.060$ ^[35] and 56.123 J K⁻¹ mol⁻¹,^[55] respectively), the temperature rise was calculated as < 41 K when we consider the heat dissipation to reactor, which is insufficient for the monitored value of 94 K (Figure 6D). As the temperature remained approximately constant during irradiation and only dropped after the light was turned off and during the control tests being irradiated by filtered light (Figure S14), the temperature increase resulted from the transformation of light energy to heat at the Ni⁰ surface, and quickly reached the equilibrium of heating and dissipation.

Based on the temperature reached at the Ni sites under full light (394 K), filtered light of $\lambda > 320$ nm (387 K), and filtered light of $\lambda > 715$ nm (334 K; Table S2b–d), the light of $320 < \lambda < 715$ nm was primarily converted to heat by absorption in accordance with the absorption spectra (Figure S6). CO₂ reduction that occurs partially owing to the contribution of warmed Ni⁰ sites converted from light energy was compared to thermal CO₂ reduction under dark conditions (Scheme 1C). At 394 and 387 K, the formation rates of C-containing products under full light were higher than the corresponding ones in dark conditions (heater used) by a factor of 15 and 5.8 times, respectively, which demonstrates the contribution of charge separation in ZrO₂ at band gap (by UV) and O vacancy (by visible light; Scheme 1A–a–d). However, IR light had no effect on CO₂ reduction (Scheme 1C).

Arrhenius-type dependence for CO₂ reduction was reported under both light and heat using ZrO₂ at the maximum formation rate of $4 \mu\text{mol h}^{-1} \text{g}_{\text{cat}}^{-1}$, for which a thermal reaction step was suggested.^[23] The present study elucidates that Ni⁰ paves the thermal route of CO to methane by the activation of H₂ and the $\frac{1}{2}kT$ value exceeding the minimum activation barrier from CO to CH₄ (Scheme 1A–d–f and B) combined with the reduction of CO₂ to CO over the ZrO₂ surface, which is driven by charge separation at the band gap and the O vacancy sites by light (Scheme 1A–a–d). Chemisorbed bicarbonate analyzed by FTIR and ¹²C ratio in products (2.0–4.3 mol %) support such efficient interplay in clear contrast to the exclusive heat reaction on the Ni surface under dark conditions. The combined promoting effects of light and heat for Ru–Cu–MgO for NH₃ decomposition may be through a similar mechanism.^[56]

Then, the interplay of light and heat steps was reconfirmed by the comparisons of kinetic tests under full light (no heat added), at 393 K under dark, and at 393 K under full light. Note that the light intensity (142 mW cm^{-2}) applied in all the experiments increased to 186 mW cm^{-2} in this comparison. In the absence of applied heat, methane formation rate increased from $330 \mu\text{mol h}^{-1} \text{g}_{\text{cat}}^{-1}$ (Figure 1C) to $1060 \mu\text{mol h}^{-1} \text{g}_{\text{cat}}^{-1}$ (Figure 7A) under full light (Table 1c, c'). Then, the methane formation rate at 393 K under dark (Figure 7B) was only 1.6% of that under UV/Vis light (Figure 7A). In contrast, when light irradiation started at 393 K, the rate increased by 190 times (Figure 7B). This demonstrates that light irradiation is essential for methane formation to activate CO₂ over ZrO₂ surface. However, methane formation rate under both light and external heat was higher by a factor of 3.2 times compared to that under light (Figure 7A,B). One of the reasons is that the reactor was homogeneously at 393 K by heater in Figure 7B while Ni⁰ nanoparticles were locally at 393 K by the heat converted from light (Figure 6D) but ZrO₂ parts in catalyst and reactor was less than 393 K due to heat dissipation. The essence of “photothermal catalysis”^[57,58] would be the interplay between photoexcited step with thermally excited step as in Scheme 1A. The photocatalysts in this paper do not need the heat from surroundings and are advantageous because light energy is converted into heat as in Scheme 1A–d–f (Figure 7A).

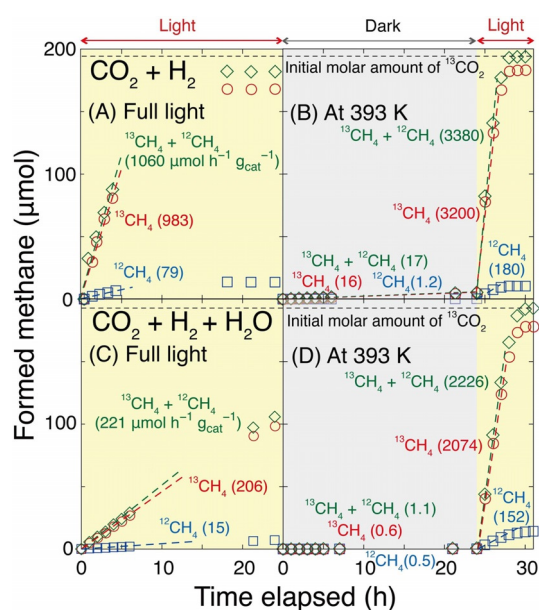


Figure 7. Time course of ¹³CH₄ and ¹²CH₄ formation during the catalytic test exposed to ¹³CO₂ (2.3 kPa) and H₂ (21.7 kPa) (A) under UV/Vis light and (B) at 393 K, under dark (first 24 h) followed by under UV/Vis light (6 h) and exposed to (C) ¹³CO₂ (2.3 kPa), H₂O (2.3 kPa), and H₂ (21.7 kPa) under UV/Vis light and (D) at 393 K, under dark (first 24 h) followed by under UV/Vis light (6 h) both using Ni (10 wt %)-ZrO₂-Reduced (0.020 g). The UV/Vis light intensity was 186 mW cm^{-2} .

Conversely, kinetic test was performed under ¹³CO₂, H₂, and full UV/Vis light through water bath to maintain the Ni (10 wt %)-ZrO₂-Reduced photocatalyst at 295 K (Table 1c'''''''). Methane was exclusively formed, however, the rate was only two times of that under dark (Table 1c'''''''), suggesting that Ni⁰ sites were cooled at ca. 295 K and negligibly proceed the hydrogenation of CO/formate (Scheme 1A–d–f). The reason why the rate was even lower than that using ZrO₂-Reduced under full light (Table 1a) would be the blocking of ZrO₂ surface and the inhibition of formed CO to desorb both by Ni nanocrystals.

Finally, we tested CO₂ photoconversion using water, H₂, and Ni (10 wt %)-ZrO₂-Reduced catalyst [Eq. (3)]. With the addition of water and H₂ to the photoreactor, the metallic Ni⁰ state was preserved and ¹³CO₂ was photoconverted into ¹³CH₄ using H₂O (Figure S16B) in dramatic contrast to test in the absence of H₂ (Supporting Information, Figure S16A). The total formation rate of C-containing products was $130 \mu\text{mol h}^{-1} \text{g}_{\text{cat}}^{-1}$ (Table 2b), which was 38% of the rate obtained using only H₂ (Table 1c). The isotopic labeling of D₂ confirmed that both water and H₂ photoreduced CO₂ into methane (Table 2c). A parent and a major fragment peak and major ¹³C-products were considered in the population analysis (Table S3). Under ¹³CO₂ (2.3 kPa), H₂ (21.7 kPa), and D₂O (2.3 kPa), ¹³CH₄ was the major product, and ¹³CH₄, ¹³CH₃D, ¹³CH₂D₂, ¹³CHD₃, and ¹³CD₄ were all steadily produced for 48 h (Figure S16C). The ratio of the formation rates was 31 300:12 500:1740:95:1, demonstrating that 8.9% of hydrogen in methane originated from water (Table 2c) in agreement with D ratio in reactant (9.6%) among D₂O and

Table 2: Kinetic data on the photoconversion of $^{13}\text{CO}_2$ (2.3 kPa) using $\text{H}_2\text{O}/\text{D}_2\text{O}$ (2.3 kPa) and/or H_2 (21.7 kPa), and Ni (10 wt%)- ZrO_2 -Reduced photocatalyst (0.020 g).^[a]

Entry	Reactant	Light irradiated	Formation rate [$\mu\text{mol h}^{-1} \text{g}_{\text{cat}}^{-1}$]						^{12}C product ratio [mol %]
			^{13}CO	^{12}CO	$^{13}\text{CH}_4$	$^{12}\text{CH}_4$	H_2	Σ products	
a	$^{13}\text{CO}_2$ and H_2O	full light	0.12	< 0.002	0.071	0.60	3.8	4.6	76
b			0.22	< 0.002	120	9.2	–	130	7.2
b'	$^{13}\text{CO}_2$, H_2O , and H_2	$\lambda > 320$ nm	0.28	< 0.002	210	15	–	220	6.7
b''			0.28	< 0.002	59	5.7	–	65	8.8
c	$^{13}\text{CO}_2$, D_2O , and H_2	full light	0.20	< 0.002	130 ^[b]	– ^[c]	–	130	– ^[c]

[a] Irradiated under UV/Vis light @142 mWcm^{-2} except for b' (186 mWcm^{-2}). [b] Including all ^{13}C -methane forms ($^{13}\text{CH}_4$, $^{13}\text{CH}_3\text{D}$, $^{13}\text{CH}_2\text{D}_2$, $^{13}\text{CHD}_3$, and $^{13}\text{CD}_4$). [c] Owing to the overlap of mass numbers, we neglected the minor ^{12}C -methane formation.

H_2 . Under these conditions, Ni^0 was the major site rather than Ni^{II} , as confirmed by EXAFS monitoring (Figure S15A, B). The formation rate of C-containing products irradiated by light at wavelength $\lambda > 320$ nm was 30 % of that irradiated by full light (Table 2b, b'), allowing the applications for conversion of CO_2 and H_2O using sunlight reached on the earth surface filtered by O_2 and O_3 layer.^[38,39] by the effects of ZrO_2 O vacancy (Scheme 1A-a-c). Furthermore, this methane formation directly from CO_2 and water is much more favorable than water electrolysis and subsequent Sabatier reaction by NASA on Mars.^[3]

The interplay of light and heat reaction steps was reconfirmed under $^{13}\text{CO}_2$, H_2 , H_2O , and UV/Vis light (186 mWcm^{-2}). In the absence of applied heat, methane formation rate increased from 130 $\mu\text{mol h}^{-1} \text{g}_{\text{cat}}^{-1}$ (Figure S16B) to 220 $\mu\text{mol h}^{-1} \text{g}_{\text{cat}}^{-1}$ (Figure 7C) under full light (Table 2b, b'). Then, the methane formation rate at 393 K under dark was essentially zero (Figure 7D). In contrast, when light irradiation started at 393 K, the rate increased by 2000 times (Figure 7D). This demonstrates that light irradiation is essential for methane formation using water as reductant.

Conclusion

Using $^{13}\text{CO}_2$, H_2 , Ni (10 wt%)- ZrO_2 -Reduced, and UV/Vis light, $^{13}\text{CH}_4$ was constantly generated at a rate of 320 $\mu\text{mol h}^{-1} \text{g}_{\text{cat}}^{-1}$ @142 mWcm^{-2} for two days, and the rate increased to 980 $\mu\text{mol h}^{-1} \text{g}_{\text{cat}}^{-1}$ @186 mWcm^{-2} . The pre-reduction of the catalyst in H_2 at 723 K was essential for the reduction of Ni species to active Ni^0 . Using FTIR spectroscopy, CO_2 was adsorbed as a bicarbonate over ZrO_2 surface and transformed to formate and then CO under the effects of charge separation in ZrO_2 . CO was reduced to methyl, and then methane on an average of 1.7 nm Ni^0 nanocrystals. Based on EXAFS, Ni^0 was reversibly heated to 394–387 K by the energy transformed from UV and/or visible light and activated H_2 and CO. The CO_2 conversion rates under UV and/or visible light was 15 and 5.8 times higher, respectively, than the corresponding temperature under dark conditions while the rate when the photoreactor was maintained in water bath @295 K was essentially equivalent to that in the dark reaction @298 K, demonstrating that the interplay of charge separation in/on ZrO_2 by light with the hydrogenation over Ni^0

surface by heat converted from light (no external heat applied) was essential for the catalytic methane formation. Using $^{13}\text{CO}_2$, H_2 , D_2O , Ni- ZrO_2 -Reduced, and UV/Vis light, $^{13}\text{CH}_4$ was constantly generated at a rate of 210 $\mu\text{mol h}^{-1} \text{g}_{\text{cat}}^{-1}$ for two days, including 8.9 % of D derived from D_2O (molar D ratio in reactant 9.6 %). This study paves the way for the utilization of first row transition metals in a reduced state utilizing sunlight reached on earth ($\lambda > 300$ nm) for solar fuel generation and ideally utilizing full spectrum of sunlight through O_3 hole or at/near stratosphere to mitigate O_3 deletion and on-site fuel supply on planets, for example, Mars.

Acknowledgements

The authors are grateful for the financial support obtained from the Grant-in-Aid for Scientific Research B (20H02834) and C (17K05961) from the Japan Society for the Promotion of Science and the Hirose Foundation (2020). X-ray absorption experiments were performed with the approval of the Photon Factory Proposal Review Committee (2020G676, 2019G141, 2018G649). The authors would like to thank Enago (<http://www.enago.jp>) for the English language review.

Conflict of interest

The authors declare no conflict of interest.

Keywords: $^{13}\text{CO}_2$ · concerted mechanism · correlated Debye model · mass chromatography · metallic nickel · zirconium oxide

- [1] Y. Izumi, *Coord. Chem. Rev.* **2013**, 257, 171–186.
- [2] “Recent Advances (2012–2015) in the Photocatalytic Conversion of Carbon Dioxide to Fuels Using Solar Energy: Feasibility for a New Energy”: Y. Izumi in *Advances in CO_2 Capture, Sequestration, and Conversion*, Vol. 1194 (Eds.: F. Jin, L.-N. He, Y. H. Hu), ACS Books, Washington, **2015**, chap. 1, pp. 1–46.
- [3] C. Vogt, M. Monai, G. J. Kramer, B. M. Weckhuysen, *Nat. Catal.* **2019**, 2, 188–197.
- [4] W. Liu, X. Li, C. Wang, H. Pan, W. Liu, K. Wang, Q. Zeng, R. Wang, J. Jiang, *J. Am. Chem. Soc.* **2019**, 141, 17431–17440.
- [5] B. Ma, G. Chen, C. Fave, L. Chen, R. Kuriki, K. Maeda, O. Ishitani, T.-C. Lau, J. Bonin, M. Robert, *J. Am. Chem. Soc.* **2020**, 142, 6188–6195.

- [6] K. E. Dalle, J. Warnan, J. J. Leung, B. Reuillard, I. S. Karmel, E. Reisner, *Chem. Rev.* **2019**, *119*, 2752–2875.
- [7] X. Li, J. Yu, M. Jaroniec, X. Chen, *Chem. Rev.* **2019**, *119*, 3962–4179.
- [8] X.-Z. Lim, *Nature* **2015**, *526*, 628–630.
- [9] H. Zhang, Y. Izumi, *Front. Chem.* **2018**, *6*, 408.
- [10] F. Li, A. Thevenon, A. Rosas-Hernández, Z. Wang, Y. Li, C. M. Gabardo, A. Ozden, C. T. Dinh, J. Li, Y. Wang, J. P. Edwards, Y. Xu, C. McCallum, L. Tao, Z.-Q. Liang, M. Luo, X. Wang, H. Li, C. P. O'Brien, C.-S. Tan, D.-H. Nam, R. Quintero-Bermudez, T.-T. Zhuang, Y. C. Li, Z. Han, R. D. Britt, D. Sinton, T. Agapie, J. C. Peters, E. H. Sargent, *Nature* **2020**, *577*, 509–513.
- [11] C.-T. Dinh, T. Burdyny, M. G. Kibria, A. Seifitokaldani, C. M. Gabardo, F. P. G. de Arquer, A. Kiani, J. P. Edwards, P. D. Luna, O. S. Bushuyev, C. Zou, R. Quintero-Bernudez, Y. Pang, D. Sinton, E. H. Sargent, *Science* **2018**, *360*, 783–787.
- [12] C. W. Li, J. Ciston, M. W. Kanan, *Nature* **2014**, *508*, 504–507.
- [13] K. Li, B. Peng, T. Peng, *ACS Catal.* **2016**, *6*, 7485–7527.
- [14] S. N. Habisreutinger, L. Schmidt-Mende, J. K. Stolarczyk, *Angew. Chem. Int. Ed.* **2013**, *52*, 7372–7408; *Angew. Chem.* **2013**, *125*, 7516–7557.
- [15] Y. Wang, Z. Zhang, L. Zhang, Z. Luo, J. Shen, H. Lin, J. Long, J. C. S. Wu, X. Fu, X. Wang, C. Li, *J. Am. Chem. Soc.* **2018**, *140*, 14595–14598.
- [16] H.-C. Hsu, I. Shown, H.-Y. Wei, Y.-C. Chang, H.-Y. Du, Y.-G. Lin, C.-A. Tseng, C.-H. Wang, L.-C. Chen, Y.-C. Lin, K.-H. Chen, *Nanoscale* **2013**, *5*, 262–268.
- [17] K. Teramura, S. Iguchi, Y. Mizuno, T. Shishido, T. Tanaka, *Angew. Chem. Int. Ed.* **2012**, *51*, 8008–8011; *Angew. Chem.* **2012**, *124*, 8132–8135.
- [18] W. A. Thompson, E. S. Fernandez, M. M. Maroto-Valer, *ACS Sustainable Chem. Eng.* **2020**, *8*, 4677–4692.
- [19] H. Zhang, T. Itoi, T. Konishi, Y. Izumi, *J. Am. Chem. Soc.* **2019**, *141*, 6292–6301.
- [20] H. Zhang, T. Itoi, K. Niki, T. Konishi, Y. Izumi, *Catal. Today* **2020**, *356*, 544–556.
- [21] Y. Kohno, T. Tanaka, T. Funabiki, S. Yoshida, *Chem. Commun.* **1997**, 841–842.
- [22] Y. Kohno, T. Tanaka, T. Funabiki, S. Yoshida, *J. Chem. Soc. Faraday Trans.* **1998**, *94*, 1875–1880.
- [23] Y. Kohno, T. Tanaka, T. Funabiki, S. Yoshida, *Phys. Chem. Chem. Phys.* **2000**, *2*, 2635–2639.
- [24] K. Sayama, H. Arakawa, *J. Phys. Chem.* **1993**, *97*, 531–533.
- [25] S. Xie, Y. Wang, Q. Zhang, W. Deng, Y. Wang, *ACS Catal.* **2014**, *4*, 3644–3653.
- [26] F. Sastre, A. V. Puga, L. Liu, A. Corma, H. García, *J. Am. Chem. Soc.* **2014**, *136*, 6798–6801.
- [27] H. Takano, Y. Kirihara, K. Izumiya, N. Kumagai, H. Habazaki, K. Hashimoto, *Appl. Surf. Sci.* **2016**, *388*, 653–663.
- [28] S. E. Collins, M. A. Baltanas, A. L. Bonivardi, *J. Catal.* **2004**, *226*, 410–421.
- [29] A. Solis-García, J. F. Louvier, A. Almedarez, J. C. Fierro, *Appl. Catal. B* **2017**, *218*, 611–620.
- [30] R. M. Silverstein, G. C. Bassler, T. C. Morrill, *Spectrometric Identification of Organic Compounds*, 4th ed., Wiley, New York, **1981**, chap. 3.
- [31] T. Schädle, B. Pejčić, B. Mizaikoff, *Anal. Methods* **2016**, *8*, 756–762.
- [32] P. A. Ussa Aldana, F. Ocampo, K. Kobl, B. Louis, F. Thibault-Starzyk, M. Daturi, P. Bazin, S. Thomas, A. C. Roger, *Catal. Today* **2013**, *215*, 201–207.
- [33] D. K. Smith, H. W. Newkirk, *Acta Crystallogr.* **1965**, *18*, 983–991.
- [34] R. E. Hann, P. R. Suitch, J. L. Pentecost, *J. Am. Ceram. Soc.* **1985**, *68*, C285–C286.
- [35] *CRC Handbook of Chemistry and Physics*, 96th ed. (Ed.: W. M. Haynes), CRC, Boca Raton, **2015**, pp. 4-124, 4-150, 12-122, 12-216.
- [36] L. Joo, T. Yu, Y. W. Kim, H. M. Park, F. Wu, J. Z. Zhang, T. Hyeon, *J. Am. Chem. Soc.* **2003**, *125*, 6553–6557.
- [37] J. Liang, Z. Deng, X. Jiang, F. Li, Y. Li, *Inorg. Chem.* **2002**, *41*, 3602–3604.
- [38] NREL website, Solar spectra (<https://www.nrel.gov/grid/solar-resource/spectra.html>, December 7, **2020**).
- [39] Y. Matsumi, M. Kawasaki, *Chem. Rev.* **2003**, *103*, 4767–4781.
- [40] M. C. Rousseaux, C. L. Ballaré, C. V. Giordano, A. L. Scopel, A. M. Zima, M. Szwarcberg-Bracchitta, P. S. Searles, M. M. Caldwell, S. B. Diaz, *Proc. Natl. Acad. Sci. USA* **1999**, *96*, 15310–15315.
- [41] J. Staehelin, N. R. P. Harris, C. Appenzeller, J. Eberhard, *Rev. Geophys.* **2001**, *39*, 231–290.
- [42] M. Diallo, B. Legras, E. Ray, A. Engel, J. A. Añel, *Atmos. Chem. Phys.* **2017**, *17*, 3861–3878.
- [43] JAXA website, Atmospheric temperature and water vapor (https://suzaku.eorc.jaxa.jp/GLI2/adeos/Earth_View/jap/adeos02j.pdf; (December 7, **2020**).
- [44] NASA website, Mars fact sheet (<https://nssdc.gsfc.nasa.gov/planetary/factsheet/marsfact.html>; December 7, **2020**).
- [45] C. L. Khodadad, G. M. Wong, L. M. James, P. J. Thakrar, M. A. Lane, J. A. Catechis, D. J. Smith, *Astrobiology* **2017**, *17*, 337–350.
- [46] G. Beni, P. M. Platzman, *Phys. Rev. B* **1976**, *14*, 1514–1518.
- [47] E. Sevillano, H. Meuth, J. J. Rehr, *Phys. Rev. B* **1979**, *20*, 4908–4911.
- [48] L. Ankudinov, B. Ravel, J. J. Rehr, S. D. Conradson, *Phys. Rev. B* **1998**, *58*, 7565–7576.
- [49] *American Institute of Physics Handbook*, 3rd ed. (Ed.: D. E. Gray), McGraw-Hill, New York, **1972**, pp. 4–116.
- [50] M. Vaarkamp, H. Linders, D. Koningsberger, *XDAP Version 2.2.7*, XAFS Services International, Woudenberg, The Netherlands, **2006**.
- [51] “Data Analysis”: D. E. Sayers, B. A. Bunker in *X-Ray Absorption—Principles, Applications, Techniques of EXAFS, SEXAFS, and XANES* (Eds.: D. C. Koningsberger, R. Prins), Wiley, New York, **1988**, p. 245.
- [52] *Springer Handbook of Condensed Matter and Materials Data* (Eds.: W. Martienssen, H. Warlimont), Springer, Heidelberg, **2005**, p. 1014.
- [53] B. J. Kip, F. B. M. Duivenvoorden, D. C. Koningsberger, R. Prins, *J. Catal.* **1987**, *105*, 26–38.
- [54] S. Calvin, M. M. Miller, R. Goswami, S.-F. Cheng, S. P. Mulvaney, L. J. Whitman, V. G. Harris, *J. Appl. Phys.* **2003**, *94*, 778–783.
- [55] M. W. Chase, Jr., *NIST-JANAF Thermochemical Tables*, 4th ed., J. Phys. Chem. Ref. Data, Monograph 9, **1998**, pp. 1–1951.
- [56] L. Zhou, D. F. Swearer, C. Zhang, H. Robotjazi, H. Zhao, L. Henderson, L. Dong, P. Christopher, E. A. Carter, P. Nordlander, N. J. Halas, *Science* **2018**, *362*, 69–72.
- [57] S. Jantarang, E. C. Lovell, T. H. Tan, J. Scott, R. Amal, *Prog. Nat. Sci. Mater. Int.* **2018**, *28*, 168–177.
- [58] C. Kim, B. L. Suh, H. Yun, J. Kim, H. Lee, *ACS Catal.* **2017**, *7*, 2294–2302.

Manuscript received: December 9, 2020

Accepted manuscript online: January 20, 2021

Version of record online: March 8, 2021